Monthly Notices
of the
ROYAL ASTRONOMICAL SOCIETY

MNRAS **437,** 547–561 (2014) doi:10.1093/mnras/stt1907
Advance Access publication 2013 November 7

A comparison of structure formation in minimally and non-minimally coupled quintessence models

Francesco Pace,[1]⋆ Lauro Moscardini,[2,3,4] Robert Crittenden,[1] Matthias Bartelmann[5] and Valeria Pettorino[6]

[1]*Institute of Cosmology and Gravitation, University of Portsmouth, Dennis Sciama Building, Portsmouth PO1 3FX, UK*
[2]*Dipartimento di Fisica e Astronomia, Universitá di Bologna, Viale Berti Pichat 6/2, I-40127 Bologna, Italy*
[3]*INFN, Sezione di Bologna, Viale Berti Pichat 6/2, I-40127 Bologna, Italy*
[4]*INAF, Osservatorio Astronomico di Bologna, via Ranzani 1, I-40127 Bologna, Italy*
[5]*Institut für Theoretische Astrophysik, Zentrum für Astronomie der Universität Heidelberg, Albert-Ueberle-Str. 2, D-69120 Heidelberg, Germany*
[6]*Département de Physique Théorique and Center for Astroparticle Physics, Université de Genève, 24 quai Ernest Ansermet, CH-1211 Genève 4, Switzerland*

Accepted 2013 October 4. Received 2013 July 26

ABSTRACT

We study structure formation in non-minimally coupled dark energy models, where there is a coupling in the Lagrangian between a quintessence scalar field and gravity via the Ricci scalar. We consider models with a range of different non-minimal coupling strengths and compare these to minimally coupled quintessence models with time-dependent dark energy densities. The equations of state of the latter are tuned to either reproduce the equation of state of the non-minimally coupled models or their background history. Thereby they provide a reference to study the unique imprints of coupling on structure formation. We show that the coupling between gravity and the scalar field, which effectively results in a time-varying gravitational constant G, is not negligible and its effect can be distinguished from a minimally coupled model. We extend previous work on this subject by showing that major differences appear in the determination of the mass function at high masses, where we observe differences of the order of 40 per cent at $z = 0$. Our new results concern effects on the non-linear matter power spectrum and on the lensing signal (differences of $\approx$10 per cent for both quantities), where we find that non-minimally coupled models could be distinguished from minimally coupled ones.

Key words: methods: analytical – cosmology: theory – dark energy.

1 INTRODUCTION

In recent years, data ranging from observations of Type Ia supernovae (Riess et al. 1998, 2004, 2007; Perlmutter et al. 1999), cosmic microwave background (CMB) and the integrated Sachs–Wolfe effect (Jaffe et al. 2001; Giannantonio et al. 2008; Ho et al. 2008; Jarosik et al. 2011; Komatsu et al. 2011; Planck Collaboration et al. 2013a,b,c), large-scale structure (LSS) and baryon acoustic oscillations (BAO; Tegmark et al. 2004; Eisenstein et al. 2005; Percival et al. 2010), globular clusters (Krauss & Chaboyer 2003), galaxy clusters (Haiman, Mohr & Holder 2001; Allen et al. 2004, 2008; Wang et al. 2004) to weak lensing (Hoekstra et al. 2006; Jarvis et al. 2006) and X-ray (Vikhlinin et al. 2009) have shown that the expansion rate of the Universe is presently accelerating. In the framework of General Relativity (GR), this can be explained by supposing that approximately three quarters of the total energetic budget of the Universe is in the form of an unknown component with negative pressure, generically known as 'dark energy.'

The simplest form of dark energy is the cosmological constant Λ, a purely geometric term in Einstein's field equations, characterized by a constant equation of state ($w = -1$) and so far in agreement with all available observations. Yet for a cosmological constant [Λ cold dark matter (ΛCDM) model], fine-tuning and coincidence problems are quite severe and remain unsolved.

An alternative is provided by quintessence scalar fields (Ratra & Peebles 1988; Wetterich 1988). The scalar field is dynamical and its background evolution is slow enough to closely reproduce the behaviour of the cosmological constant and drive the accelerated expansion today. However observations constrain quite tightly the equation of state of the dark energy component to be very close to -1 at present (Komatsu et al. 2011) and in this case, as pointed out by Bludman (2004), the basin of attraction in the early universe is shrinking and thus enhancing the fine tuning present in minimally quintessence models, as severe as the ΛCDM one.

Given these considerations, it is worth investigating extensions of GR in which dark energy is associated with a scalar field

⋆ E-mail: francesco.pace@port.ac.uk

non-minimally coupled to gravity. In these extended models, the field dynamics may differ from that of minimally coupled models due to gravitational effects. In such scenarios, the scalar field mediates a *fifth force*; this happens when there is a universal coupling to all species, as in scalar–tensor theories (Hwang 1991; Demarque et al. 1994; Barrow 1996; Mashhoon, Wesson & Liu 1998; Boisseau et al. 2000; Faraoni 2000; Perrotta, Baccigalupi & Matarrese 2000; Torres 2002; Fujii & Maeda 2003; Banerjee & Ganguly 2009; Charmousis et al. 2012; Jamil, Raza & Debnath 2012; Wang, Hui & Khoury 2012), or if the coupling is non-universal, as it happens in coupled quintessence (Schmidt 1990; Wetterich 1995; Amendola 2000, 2004; Holden & Wands 2000; Sidharth 2000; Amendola et al. 2003, 2012; Matarrese, Pietroni & Schimd 2003; Amendola, Baldi & Wetterich 2008; Guendelman & Kaganovich 2008; Mota, Shaw & Silk 2008; Pettorino & Baccigalupi 2008; Baldi et al. 2010; Zhao et al. 2010; Pettorino et al. 2010, 2012); it also occurs with physics associated with generalized kinetic energy terms (Armendariz-Picon, Mukhanov & Steinhardt 2001; Caldwell 2002; Malquarti, Copeland & Liddle 2003). One effect of this class of models is that the gravitational constant G, appearing in Einstein's field equations is no longer a constant, but becomes a function of the scalar field and thus becomes time dependent.

In scalar–tensor theories the scalar field is non-minimally coupled to gravity via the Ricci scalar and at present times can behave as dark energy. Models with this coupling are also called extended quintessence models (Perrotta et al. 2000; Acquaviva, Baccigalupi & Perrotta 2004; Acquaviva et al. 2005; Pettorino, Baccigalupi & Perrotta 2005b; Pettorino & Baccigalupi 2008). One of the consequences of these models is that the coupling of the scalar field to the Ricci scalar in the Lagrangian enhances the dynamics of the field at early times, an effect known as R-boost (Baccigalupi, Matarrese & Perrotta 2000; Pettorino, Baccigalupi & Mangano 2005a). As a consequence the range of attraction for tracking solutions is conserved also for models where the equation of state is close to -1 today (Matarrese, Baccigalupi & Perrotta 2004). Fine tuning is however still present in the choice of a flat potential.

In this paper we investigate the effects of extended quintessence models on structure formation from an analytical point of view, thus complementing, validating and extending the work based on N-body numerical simulations by De Boni et al. (2011). The novelty of this work is the study of the spherical collapse in scalar–tensor theories (Bernardeau 1994; Esposito-Farèse & Polarski 2001; Ohta, Kayo & Taruya 2003, 2004; Acquaviva et al. 2004; Mota & van de Bruck 2004; Perrotta et al. 2004; Nunes & Mota 2006; Abramo et al. 2007; Pettorino & Baccigalupi 2008; Basilakos, Sanchez & Perivolaropoulos 2009; Basilakos, Plionis & Solà 2010; Pace, Waizmann & Bartelmann 2010; Wintergerst & Pettorino 2010). To this purpose we generalize the semi-analytical spherical collapse model to take into account effects from the scalar field (which, for simplicity, is considered to be homogeneous) in order to study the time behaviour of the linearly extrapolated density contrast $\delta_{\rm c}$ and the linear growth factor. We will study five minimally coupled dark energy models, two of which with the same equation of state parameter of the simulated extended quintessence models and two with an equation of state tuned to reproduce the same background history of the simulated non-minimally coupled models.

The paper is organized as follows. In Section 2 we present the models studied in this work and we describe how to take into account the scalar field for perturbation theory in the quasi-static Newtonian regime in scalar–tensor theories. In Section 3 we present our results for the linear growth factor (Section 3.1), the spherical collapse parameters $\delta_{\rm c}$ and Δ_V (Section 3.2), the mass function (Section 3.3), the non-linear matter power spectrum (Section 3.4) and the cosmic shear power spectrum (Section 3.5). Finally, Section 4 is devoted to our conclusions. Throughout we work in units where the speed of light is $c = 1$.

2 COSMOLOGICAL MODELS

2.1 ΛCDM and quintessence dark energy models

In this work we will consider as fiducial model the ΛCDM model, characterized by the presence of a cosmological constant described by an equation of state $w = -1$, constant at all times. This implies that the amount of dark energy will not change and eventually comes to dominate the total energy density. In other dark energy models we consider, the equation of state parameter is in general a function of time. In a homogeneous and isotropic universe, the cosmological expansion can be written in terms of the first Friedmann equation

$$H^2 = H_0^2 \left[\Omega_{\rm r,0} a^{-4} + \Omega_{\rm m,0} a^{-3} + \Omega_{\rm K,0} a^{-2} + \Omega_{\rm q,0} g_{\rm q}(a)\right], \tag{1}$$

where $\Omega_{\rm r,0}$ represents the radiation, $\Omega_{\rm m,0}$ the matter, $\Omega_{\rm K,0}$ the curvature and $\Omega_{\rm q,0}$ the dark energy densities today, respectively. The function $g(a)$ describes the time evolution of the dark energy density component. For a perfect fluid, where the pressure (P) and energy density (ρ) are related by some dark energy equation of state, $P = w(a)\rho$, $g_{\rm q}(a)$ is

$$g_{\rm q}(a) = \exp\left(-3\int_1^a \frac{1 + w(a')}{a'}{\rm d}a'\right). \tag{2}$$

As one can easily see from equation (2), for the cosmological constant $g_{\rm q}(a) = 1$.

The idea of replacing the cosmological constant by the energy density of a scalar field was explored in several works (Wetterich 1985, 1988, 1995; Ratra & Peebles 1988) and if the scalar field does not experience any direct coupling to any of the other constituents of the models it is said to be minimally coupled and the action reads

$$S = \int {\rm d}^4x\sqrt{-g}\left(\frac{R}{16\pi G} + \mathcal{L}_\phi + \mathcal{L}_{\rm fl}\right), \tag{3}$$

where g is the determinant of the metric, R the Ricci scalar, $\mathcal{L}_{\rm fl}$ is the Lagrangian of all fluids except the dark energy scalar field and $\mathcal{L}_\phi$ represents the Lagrangian of the scalar field:

$$\mathcal{L}_\phi = -\frac{1}{2}\nabla^\mu\phi\nabla_\mu\phi - V(\phi), \tag{4}$$

where $V(\phi)$ denotes the self-interaction potential of ϕ. Below we will generally assume the potential takes the *Ratra–Peebles* form,

$$V(\phi) = \frac{M^{4+\alpha}}{\phi^\alpha}, \tag{5}$$

where M is a typical energy scale and α is a free positive exponent.

Varying the action in equation (3) with respect to the metric $g_{\mu\nu}$ gives the usual Einstein field equations

$$\boldsymbol{G}_{\mu\nu} = 8\pi G\left[\boldsymbol{T}^{(\rm fl)}_{\mu\nu} + \boldsymbol{T}^{(\phi)}_{\mu\nu}\right], \tag{6}$$

where $\boldsymbol{G}_{\mu\nu}$ is the Einstein tensor, $\boldsymbol{T}^{(\rm fl)}_{\mu\nu}$ is the stress-energy tensor for a homogeneous and isotropic cosmic fluid (here dominated by dark matter) and $\boldsymbol{T}^{(\phi)}_{\mu\nu}$ is the stress-energy tensor for the quintessence scalar field:

$$\boldsymbol{T}^{(\phi)}_{\mu\nu} = \nabla_\mu\phi\nabla_\nu\phi - g_{\mu\nu}\left(\frac{1}{2}\nabla^\alpha\phi\nabla_\alpha\phi + V(\phi)\right). \tag{7}$$

Assuming a spatially flat Friedmann–Robertson–Walker (FRW) metric $\mathrm{d}s^2 = -\mathrm{d}t^2 + a^2(t)\,\mathrm{d}\boldsymbol{x}^2$ where $a(t)$ is the scale factor we can identify the energy density and pressure of the scalar field as

$$\rho_\phi = \frac{1}{2}\dot{\phi}^2 + V(\phi), \tag{8}$$

$$p_\phi = \frac{1}{2}\dot{\phi}^2 - V(\phi). \tag{9}$$

Varying the action S with respect to the scalar field itself we derive the equations of motion which resemble the Klein–Gordon equation for a spatially homogeneous field on an isotropically expanding space–time:

$$\ddot{\phi} + 3H\dot{\phi} + \frac{\mathrm{d}V(\phi)}{\mathrm{d}\phi} = 0. \tag{10}$$

With the assumption of a flat FRW metric, the scalar field satisfies the continuity equation

$$\dot{\rho}_\phi + 3H(\rho_\phi + p_\phi) = 0, \tag{11}$$

so that we can write $\rho_\phi = \rho_{\phi,0} g_\mathrm{q}(a)$, with $g_\mathrm{q}(a)$ defined in equation (2).

2.2 Scalar–tensor models

Scalar–tensor (sometimes called extended quintessence) models are instead described by the action

$$S = \int \mathrm{d}^4x\sqrt{-g}\left(\frac{1}{2}f(\phi, R) + \mathcal{L}_\phi + \mathcal{L}_\mathrm{fl}\right), \tag{12}$$

where this formulation was first introduced in a cosmological context by Hwang (1991). With respect to GR, the term $R/16\pi G$ is replaced by an arbitrary function of the Ricci scalar and scalar field $f(\phi, R)/2$. In addition, the scalar field is described by the Lagrangian

$$\mathcal{L}_\phi = -\frac{1}{2}\omega(\phi)\nabla^\mu\phi\nabla_\mu\phi - V(\phi), \tag{13}$$

where $\omega(\phi)$ is a function of the scalar field only which generalizes the kinetic term.

These models are interesting because they are related to the original Brans–Dicke idea (Brans & Dicke 1961) and to the attempt to explain cosmic acceleration exclusively in terms of modifications of GR. Such models have been studied in several works (see also Wetterich 1995; Barrow & Parsons 1997; Sahni & Habib 1998; Uzan 1999; Bartolo & Pietroni 2000; Boisseau et al. 2000; Faraoni 2000; Perrotta et al. 2000; Esposito-Farèse & Polarski 2001; Perrotta & Baccigalupi 2002; Torres 2002; Linder 2004; Matarrese et al. 2004; Pettorino et al. 2005a; Pettorino & Baccigalupi 2008; Tsujikawa et al. 2008; Boisseau 2011; Bueno Sánchez & Perivolaropoulos 2011; Charmousis et al. 2012; Jamil et al. 2012; Wang et al. 2012). Here we just summarize the most important aspects that will be relevant for the present work.

The variation of the action described in equation (12) with respect to the metric $g_{\mu\nu}$ yields the field equations

$$\boldsymbol{G}_{\mu\nu} = 8\pi G\boldsymbol{T}_{\mu\nu} = \frac{1}{f'}\left[\boldsymbol{T}^{(fl)}_{\mu\nu} + \boldsymbol{T}^{(\phi)}_{\mu\nu} + \frac{1}{2}g_{\mu\nu}(f - f'R) + \boldsymbol{A}_{\mu\nu}(f')\right], \tag{14}$$

where the tensor $\boldsymbol{A}_{\mu\nu}$ is defined for an arbitrary scalar h as

$$\boldsymbol{A}_{\mu\nu}(h) = \nabla_\mu\nabla_\nu h - g_{\mu\nu}\Box h, \tag{15}$$

and $f' \equiv \partial f/\partial R$. The Klein–Gordon equation for the scalar field is also modified with respect to the minimally coupled case,

$$\ddot{\phi} + 3H\dot{\phi} = -\frac{1}{2\omega}\left(\frac{\mathrm{d}\omega}{\mathrm{d}\phi}\dot{\phi}^2 - \frac{\partial f}{\partial\phi}R + 2\frac{\mathrm{d}V}{\mathrm{d}\phi}\right). \tag{16}$$

The energy-momentum tensor for the scalar field now reads

$$\boldsymbol{T}^{\phi}_{\mu\nu} = \omega(\phi)\left(\nabla_\mu\phi\nabla_\nu\phi - \frac{1}{2}g_{\mu\nu}\nabla^\alpha\phi\nabla_\alpha\phi\right) - g_{\mu\nu}V(\phi), \tag{17}$$

and it is interesting to note that, unlike in the minimally coupled models, these modifications imply that the energy density of the scalar field no longer satisfies the continuity equation for the background quantities ($\dot{\rho} + 3H(\rho + p) = 0$) (Hwang 1991).

We assume that $f(\phi, R)$ is linear in the Ricci scalar,

$$f(\phi, R) = \frac{F(\phi)}{8\pi G_*}R, \tag{18}$$

then by identifying the energy-momentum tensor of the scalar field with that of a perfect fluid, we can derive expressions for the non-conserved background energy density and pressure of the scalar field:

$$\rho_\phi = \frac{1}{2}\omega(\phi)\dot{\phi}^2 + V(\phi) - 3H\dot{F}(\phi), \tag{19}$$

$$p_\phi = \frac{1}{2}\omega(\phi)\dot{\phi}^2 - V(\phi) + \ddot{F}(\phi) + 2H\dot{F}(\phi). \tag{20}$$

These models can be related to the original Brans–Dicke gravity (Brans & Dicke 1961) when $F = \phi$ and $\omega(\phi) = \omega_\mathrm{BD}\phi$, while non-minimally coupled theories are obtained with the identifications $\omega(\phi) = F(\phi) = 1$.

With this linear ansatz for $f(\phi, R)$, Friedmann's equations become

$$H^2 = \frac{8\pi G}{3F}\left(\rho_\mathrm{fl} + \frac{1}{2}\dot{\phi} + V(\phi) - 3H\dot{F}\right), \tag{21}$$

$$\frac{\ddot{a}}{a} = -\frac{4\pi G}{3F}\left[\rho_\mathrm{fl} + 3p_\mathrm{fl} + 2\dot{\phi}^2 - 2V(\phi) - 3(\ddot{F} + H\dot{F})\right]. \tag{22}$$

If we define an effective Jordan–Brans–Dicke parameter as

$$\omega_\mathrm{JBD} = \frac{F(\phi)}{(F_{,\phi}(\phi))^2}, \tag{23}$$

then GR is recovered when $\omega_\mathrm{JBD} \gg 1$.

Any changes to the gravitational physics require matching the GR behaviour on Solar system scales where gravity is well tested, while still reproducing the observed effects of dark energy on large scales. Here we require that

$$f(\phi_0, R) = \frac{R}{8\pi G}, \tag{24}$$

where ϕ_0 is the value of the scalar field today and G is the gravitational constant measured today. In the following we will assume the modifications take the following form:

– $\omega(\phi) = 1$,

– $F(\phi) = 1 + 8\pi G_*\xi(\phi^2 - \phi_0^2)$,

where ξ is the coupling constant, and ϕ_0 is the present value of the scalar field. G_* is the bare gravitational constant (Esposito-Farèse & Polarski 2001) which in general differs from the gravitational constant G appearing in Einstein's or Newton's field equations.

Very tight constraints ($\xi \approx 10^{-2}$) on the coupling parameter come from Solar system tests (Reasenberg et al. 1979; Chiba 1999;

Table 1. Values of the parameters adopted for the reference ΛCDM model and the dynamical dark energy models. The exponent of the inverse power-law potential is indicated with α, ξ is the strength of the coupling, $\omega_{\rm JBD,0}$ is the present value of the effective Jordan–Brans–Dicke parameter and σ_8 represents the normalization of the matter power spectrum such that fluctuations are the same at $z_{\rm CMB}$.

Model	α	ξ	$\omega_{\rm JBD,\,0}$	σ_8
ΛCDM	–	–	–	0.776
NMC1	0.229	+0.085	120	0.748
NMC2	0.435	−0.072	120	0.729
MCw1	–	–	–	0.752
MCw2	–	–	–	0.745
MCH1	–	–	–	0.744
MCH2	–	–	–	0.760
wCDM	–	–	–	0.753

Uzan 1999; Will 2001; Riazuelo & Uzan 2002; Bertotti, Iess & Tortora 2003), from cosmological scale measurements (Acquaviva et al. 2005; Clifton, Barrow & Scherrer 2005; Appleby & Weller 2010; Farajollahi, Salehi & Nasiri 2011) and nucleosynthesis (Accetta, Krauss & Romanelli 1990; Torres 1995; Santiago, Kalligas & Wagoner 1997; Coc et al. 2006; Lee 2011). These works assume no screening mechanism, while other works assume screening, either exploiting the chameleon effect (Khoury & Weltman 2004; Mota & Barrow 2004) or the Vainshtein mechanism (Vainshtein 1972). Many simulations now take into account such screening mechanism (Oyaizu 2008; Schmidt 2009; Zhao, Li & Koyama 2011).

2.3 Model parameters

We will compare analytic results presented in Section 3.3 with *N*-body simulations discussed in De Boni et al. (2011). To do so, we adopt the *Wilkinson Microwave Anisotropy Probe* (*WMAP*; Spergel et al. 2007) cosmological parameters which had been used in these simulations ($\Omega_{\rm m,0} = 0.268$, $\Omega_{\phi,0} = 0.732$, $h_0 = 0.704$) and throughout the paper we assume a spatially flat cosmological background, $\Omega_{\rm K,0} = 0$. These parameters are slightly different from the ones found by *Planck*,[1] but here we want to emphasize the comparison of models having the same cosmological parameters, therefore, this does not represent an issue for the conclusions of our work.

We consider two non-minimally coupled models and five minimally coupled models (see Table 1). These models are labelled NMC*n*, MCw*n* or MCH*n*, respectively, where the index *n* runs from one to two. The non-minimally coupled models differ essentially in their coupling strengths. They correspond to the maximum deviation from GR allowed by current observations on cosmological scales. The minimally coupled models MCw1 and MCw2 have the same equation of state as the simulated extended quintessence models (NMC1 and NMC2) and the minimally coupled models MCH1 and MCH2 have the same background history of the models NMC1 and NMC2 in order to independently evaluate the effect of the coupling and of the time-dependent gravitational constant. A fifth model, wCDM, has a constant equation of state parameter $w = -0.9$, the highest value consistent with observational constraints (Unnikrishnan & Seshadri 2008).

[1] planck.esa.int/

We normalize the amplitude of the primordial power spectrum for the fiducial ΛCDM cosmology to have a value of the quadratic deviation on a comoving scale of 8 Mpc h^{-1} of $\sigma_8 = 0.776$. Dark energy models are normalized to match the amplitude of fluctuations at the CMB epoch $z_{\rm CMB} = 1089$ according to the relation

$$\sigma_{8,\rm DE} = \sigma_{8,\Lambda\rm CDM}\frac{D_{+,\Lambda\rm CDM}(z_{\rm CMB})}{D_{+,\rm DE}(z_{\rm CMB})}. \tag{25}$$

In the previous equation $D_+(z)$ is the linear growth factor normalized to unity today (see Section 3.1). An alternative normalization which is often adopted in the literature is to fix the exponential tail of the mass function to be approximately the same at $z = 0$; therefore, differences will arise at earlier times. However, since the normalization of the fluctuations is bounded to high accuracy by the CMB measurements, we exclusively adopt the first normalization. The values of the parameters for the extended quintessence models are chosen so that the energy density of the scalar field today is approximately the same as that of the cosmological constant. The other differences arising at $z = 0$ may be used to discriminate among the different cosmological models.

In Fig. 1 we show the redshift evolution of the equation of state w (upper panel) and of the function $1/F(\phi)$ (lower panel) for the quintessence models studied in this work. We refer to the caption for the different colours and line styles adopted. The value of the equation of state at $z = 0$ is close to $w = -0.9$ for all the dynamical models investigated, except for the models MCH1 and MCH2. The equations of state become essentially constant for $z > 3$. The minimally coupled dark energy models MCw1 and MCw2 are described by the same w as models NMC1 ($\xi = 0.085$) and NMC2 ($\xi = -0.072$). The equation of state for the minimally coupled models MCH*n* is derived using the following expression:

$$w(a) = -\frac{1 + \frac{2}{3}a\frac{{\rm d}\ln E(a)}{{\rm d}a} + \frac{1}{3}\frac{\Omega_{\rm r}}{a^4E(a)^2} - \frac{1}{3}\frac{\Omega_{\rm K,0}}{a^2E(a)^2}}{1 - \frac{\Omega_{\rm m,0}}{a^3E(a)^2} - \frac{\Omega_{\rm r}}{a^4E(a)^2} - \frac{\Omega_{\rm K,0}}{a^2E(a)^2}}, \tag{26}$$

where $H(a) = H_0E(a)$.

The function $F(\phi)$ changes rapidly at low redshifts and becomes practically constant for $z \gtrsim 2$, differing from the minimally coupled case by at most 2.5 per cent. Since in the field equations the usual gravitational constant G is replaced by the function $1/F(\phi)$, according to the sign of the coupling constant, gravity will be stronger ($\xi > 0$) or weaker compared ($\xi < 0$) to the minimally coupled case. This happens because of the functional form of $F(\phi) = 1 + 8\pi G_*\xi(\phi^2 - \phi_0^2)$.

2.4 Background properties

As the values of the coupling constants are small, we expect small differences at the background level between these models and the reference ΛCDM model. Our expectations are confirmed by Fig. 2 where we show the ratio of the scalar field density and the Hubble parameter (upper and lower panel, respectively) as a function of redshift for the eight models considered here with respect to the cosmological constant model. For the Hubble parameter, the maximum difference, ≈4 per cent, takes place at $z \approx 1$. These differences in the Hubble function render the differences in the age of the Universe or in distances to be very small, of the order of a few per cent. Similar differences are present in the comoving and in the luminosity distance. Ratios of the matter density fraction will be simply related to the corresponding Hubble functions.

Since the Hubble parameter is a key ingredient in determining the time evolution of the perturbations, we can infer that they will

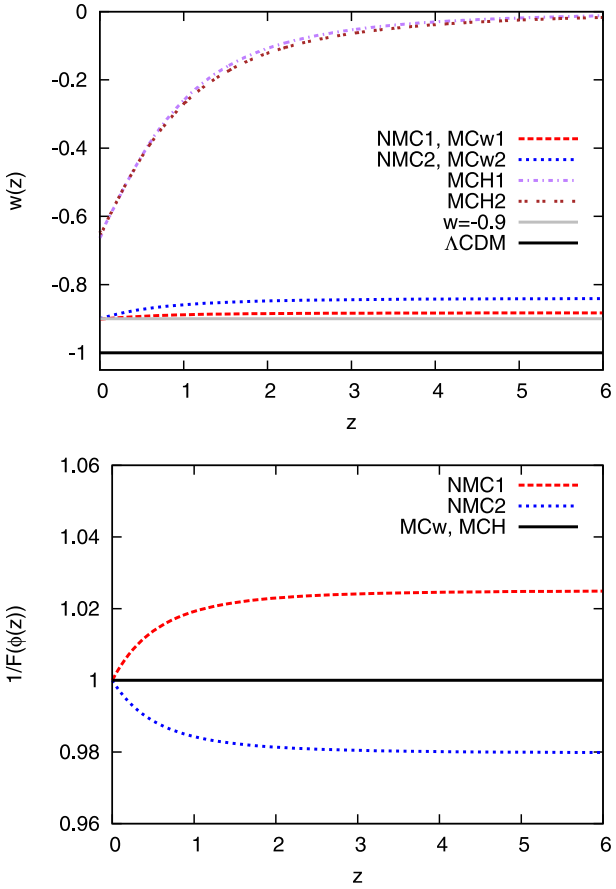

Figure 1. Upper panel: equation of state for the dark energy models considered in this work as a function of redshift. Lower panel: redshift dependence of the function $F^{-1}(\phi) \simeq 1 - 8\pi G_* \xi(\phi^2 - \phi_0^2)$. The red dashed curve represents the model NMC1 with coupling constant $\xi = 0.085$, the blue short dashed curve represents the model NMC2 with coupling constant $\xi = -0.072$. The two minimally coupled models MCw1 and MCw2 have the same equation of state parameter of the extended quintessence models NMC1 and NMC2 and are shown with the same curve. Models MCH1 and MCH2 are shown with violet short dashed–dotted and brown dot–dotted line. Finally, the reference ΛCDM ($w = -1$) and wCDM ($w = -0.9$) models are shown with a black and grey solid line, respectively.

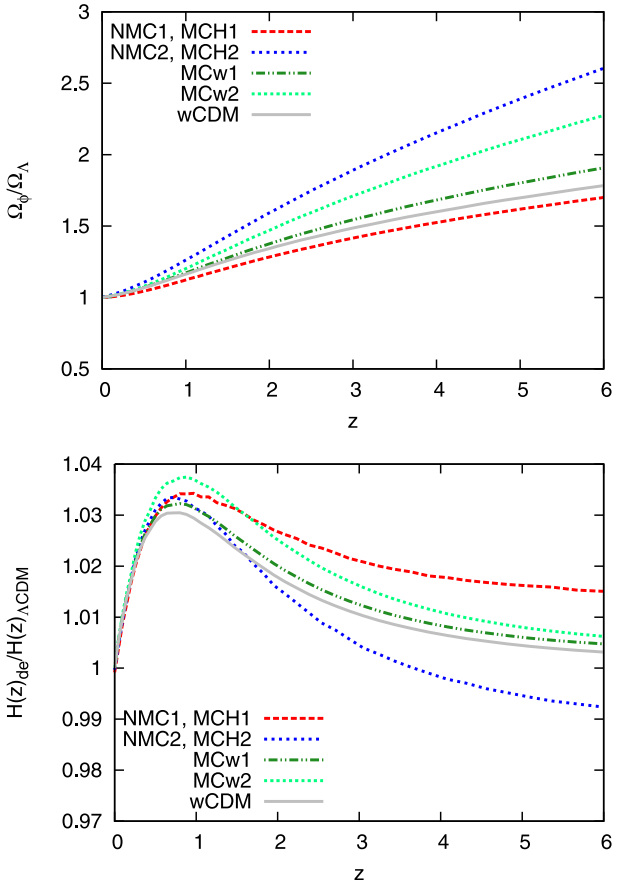

Figure 2. Upper (lower) panel: redshift evolution of the ratio of the scalar field (Hubble) parameter for the different models studied to the corresponding quantity in the fiducial ΛCDM model. Line types and colours for the non-minimally coupled models are as in the upper panel of Fig. 1. Models MCw1 and MCw2 are shown with dark dot–dashed-dotted and light green dotted curves, respectively.

not substantially differ from results expected in the ΛCDM case, as explained in detail in the following sections.

It is worth noticing that the minimally coupled models MCw1, MCw2 and wCDM have very similar expansion histories, while the other models differ more. This is due to the fact that they are characterized by the same coupling constant, and arises despite the fact that the dark energy equations of state are explicitly tuned to match. This shows the importance, already at the background level, of the coupling constant. In fact we can also see from the lower panel of Fig. 2 that models having the same coupling constants show very similar expansion histories and time evolutions of the matter content.

2.5 Perturbations

We now review the main features of linear perturbation theory within non-minimally coupled cosmologies in the Newtonian limit. For an extended review we refer the reader to Pettorino & Baccigalupi (2008) and Wintergerst & Pettorino (2010).

In the Newtonian limit, time derivatives are negligible with respect to spatial derivatives and the condition $k \gg H$ holds. In other words we are considering a quasi-static regime and that scales of interest are much smaller than the horizon. In this limit, the perturbed continuity, Euler and Poisson equations are (in comoving coordinates)

$$\dot{\delta} = -\nabla_x \cdot \boldsymbol{u}, \tag{27}$$

$$\frac{\partial \boldsymbol{u}}{\partial t} = -2H\boldsymbol{u} - \frac{1}{a^2}\nabla_x \psi, \tag{28}$$

$$\nabla_x^2 \phi_{\rm E} = \frac{4\pi G}{F}\bar{\rho}_{\rm m}\Omega_{\rm m}\delta, \tag{29}$$

where δ is the matter perturbation, $\boldsymbol{u}$ the comoving peculiar velocity and ψ is the Newtonian gravitational potential. The potential $\phi_{\rm E}$ appearing in the Poisson equation is defined as

$$\phi_{\rm E} = \left(1 + \frac{1}{2}\frac{F_{,\phi}^2}{F + F_{,\phi}^2}\right)\phi. \tag{30}$$

The Poisson equation can be rewritten also in terms of the gravitational potential $\psi_{\rm E}$:

$$\nabla_x^2 \psi_{\rm E} = -\frac{4\pi G}{F}\bar{\rho}_{\rm m}\Omega_{\rm m}\delta, \tag{31}$$

where $\psi_{\rm E}$ is defined as

$$\psi_{\rm E} = \left(1 - \frac{1}{2}\frac{F_{,\phi}^2}{F + 2F_{,\phi}^2}\right)\psi. \tag{32}$$

The Euler equation can therefore be modified to

$$\frac{\partial \boldsymbol{u}}{\partial t} + 2H\boldsymbol{u} + \left(1 + \frac{F_{,\phi}^2}{F + F_{,\phi}^2}\right)\nabla_x\phi = 0. \tag{33}$$

Combining now all the three equations, we obtain a second-order differential equation describing the time evolution of the linear growth factor:

$$\ddot{\delta} + 2H\dot{\delta} - 4\pi G_{\rm eff}\bar{\rho}_{\rm m}\delta = 0, \tag{34}$$

where $G_{\rm eff}$ is defined as (see also Esposito-Farèse & Polarski 2001)

$$G_{\rm eff} = \frac{G}{F}\frac{2(F + F_{,\phi}^2)}{2F + 3F_{,\phi}^2} \approx \frac{G}{F} \tag{35}$$

for $\xi \ll 1$.

As the coupling constant is $\xi \ll 1$, in our models, we can use the approximation $G_{\rm eff} = G/F$. The equation for the growth factor is similar the one obtained in $f(R)$ models. This approximation is valid since, in our models, $F_{,\phi}/F \ll 1$.

3 RESULTS

In this section we will present results concerning structure formation for the quintessence models described above in both the linear and non-linear regimes. In particular we study the growth factor (Section 3.1), the linear and non-linear overdensity parameter (Section 3.2), the mass function (Section 3.3), the analytical non-linear dark matter power spectrum (Section 3.4) and the cosmic shear power spectrum (Section 3.5).

3.1 Growth factor

The linear growth factor has been extensively studied in several works (see e.g. Copeland, Sami & Tsujikawa 2006; Perivolaropoulos 2007; Pettorino & Baccigalupi 2008; Tsujikawa et al. 2008; Bueno Sánchez & Perivolaropoulos 2011; Lee 2011). In Fig. 3 we show the growth factor divided by the scale factor $(D_+(a)/a)$ for the dark energy models considered in this work, as compared to the fiducial ΛCDM model. We show two normalizations for the fluctuations, matching the amplitudes at the present time ($z = 0$) or at the last scattering of the CMB (see e.g. Bartelmann, Doran & Wetterich 2006).

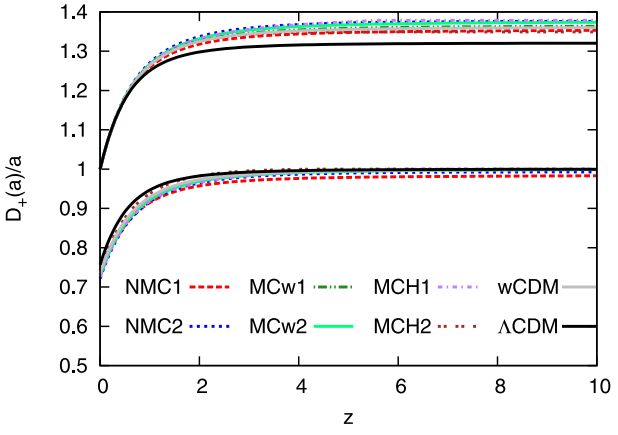

Figure 3. The linear growth factor divided by the scale factor $D_+(a)/a$ as a function of the redshift. Upper (lower) curves show the linear growth factor normalized to unity today (at the CMB epoch). Line styles and colours for the quintessence models are the same as in Fig. 2, while the fiducial ΛCDM model is shown with the solid black line.

We observe that differences between the dark energy models and the ΛCDM model are of few per cent, ranging between 2 per cent for the NMC1 model and 5 per cent for the NMC2 model. The minimally coupled model MCH1 (MCH2) behaves very similarly to the non-minimally coupled model NMC2 (NMC1). This is easily explained taking into account that the source term in equation (34) is modified by the coupling function $F(\phi)$ and this function compensates the differences in the background expansion history. Generally, the quintessence models show less growth compared to the ΛCDM model. When the growth factor is normalized to unity now, primordial perturbations have to be higher to give the same number of structures today. When instead the growth factor is normalized to unity at early times, the growth factor is lower because the higher amount of dark energy slows down structure growth.

The study of the growth factor is relevant also for the evaluation of the integrated Sachs–Wolfe (ISW; Sachs & Wolfe 1967) and of the Rees–Sciama (RS) effects (Rees & Sciama 1968). The ISW effect is due to the interaction of CMB photons with a time varying gravitational potential. The relative change of the CMB temperature is given by

$$\tau = \frac{\Delta T}{T_{\rm CMB}} = \frac{2}{c^3}\int_0^{\chi_{\rm H}} {\rm d}\chi a^2 H(a)\frac{\partial}{\partial a}(\Phi - \Psi), \tag{36}$$

where $\chi_{\rm H}$ is the horizon distance. The gravitational potentials are related to each other (equations 30 and 32) and via the Poisson equation (equation 31) to the matter overdensity. The ISW effect is therefore proportional to the quantity ${\rm d}(D_+(a)/a)/{\rm d}a$, where $D_+(a)$ is the growth factor. Here we are in particular interested in the late ISW effect because it is affected by the dark energy dynamics.

The RS effect is similar to the ISW, but includes non-linear evolution of the gravitational potentials, which we include to second order, following Schäfer (2008). The ISW effect depends on the time derivative of the gravitational potential Φ that via Poisson's equation is related to the overdensity δ: $\nabla^2\Phi \propto \delta$. It is therefore possible to replace the gravitational potential with the overdensity itself simply inverting Poisson's equation: $\Phi \propto \triangle^{-1}\delta$. Expanding the overdensity as $\delta = D_+(a)\delta^{(1)} + D_+^2(a)\delta^2$ we obtain the desired expression for the RS effect.

The ISW and RS effects are shown in Fig. 4 where, for clarity, we present differences between the cosmological models we considered and the ΛCDM model. The upper panel shows the ISW effect, the lower panel the RS effect. The largest differences between models occur at $z \approx 1$ and are of the order of 10 per cent. As expected, the largest differences arise for the different couplings, while the non-minimally coupled dark energy models are all very similar to each other.

As we can see from Fig. 4, at early times when the dark energy contribution is negligible, all the models approximate the EdS model. We will therefore have that $D_+(a) \propto a$, hence the ISW vanishes while the RS effect approaches an asymptotic value. This might appear surprising since non-minimally coupled models are characterized by a non-negligible amount of dark energy at early times. However, for the models we consider, the coupling constant is very small and the amount of dark energy at early times is negligible, as it is evident from Fig. 5.

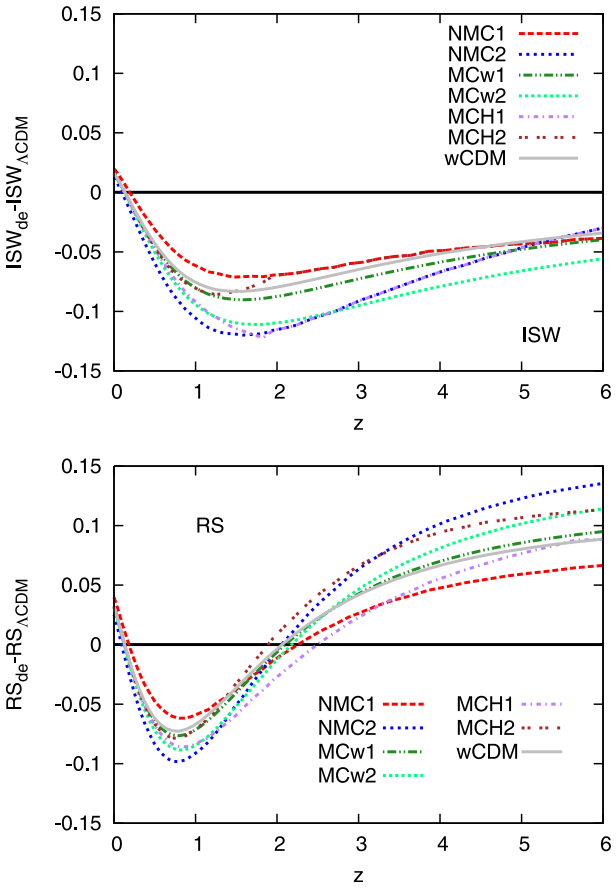

Figure 4. Upper (lower) panel: redshift evolution of the difference for the quantity characterizing the ISW (Rees–Sciama) signal between the dark energy models and the ΛCDM one. Line styles and colours for the quintessence models are the same as in Fig. 3.

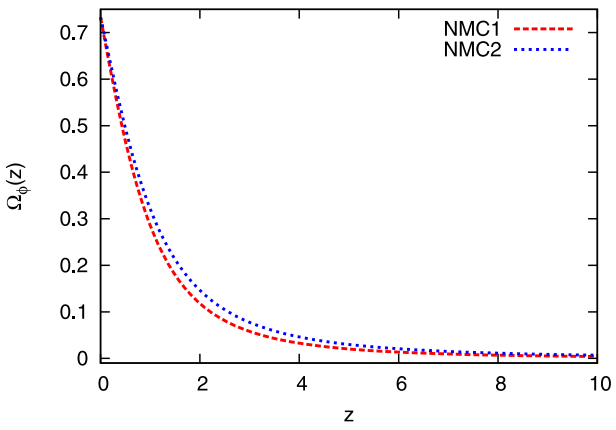

Figure 5. Amount of dark energy for the non-minimally coupled models as a function of redshift z. Line styles and colours are as in Fig. 1.

3.2 Spherical collapse

We next summarize theoretical arguments required to evaluate the spherical collapse parameters δ_c (the linear evolution overdensity parameter) and Δ_V (the virial overdensity parameter).

In the spherical collapse model, objects forming under gravitational collapse of matter overdensities are assumed to be non-rotating and spherical. Even though this is clearly a crude assumption, since cosmic structures originate from the primordial seeds are triaxial and rotating (Shaw et al. 2006; Bett et al. 2007), the model provides predictions that can reproduce the results of numerical simulations quite well. Spherical collapse has been analysed in the literature very extensively (see e.g. Bernardeau 1994; Ohta et al. 2003, 2004; Mota & van de Bruck 2004; Nunes & Mota 2006; Abramo et al. 2007; Basilakos et al. 2009, 2010; Pace et al. 2010; Wintergerst & Pettorino 2010); to study perturbations in non-minimally coupled models we will follow closely (Esposito-Farèse & Polarski 2001; Acquaviva et al. 2004; Perrotta et al. 2004; Pettorino & Baccigalupi 2008).

In order to derive the differential equation describing the time evolution of the linear overdensity factor, we can simply repeat the derivation described above (Section 2.5), taking into account the full non-linearity of the continuity and Euler equations. Doing so, the continuity and Euler equations read

$$\dot{\delta} + (1+\delta)\nabla_x \cdot \boldsymbol{u} = 0, \tag{37}$$

$$\frac{\partial \boldsymbol{u}}{\partial t} + 2H\boldsymbol{u} + (\boldsymbol{u}\cdot\nabla_x)\boldsymbol{u} + \frac{1}{a^2}\nabla_x\psi = 0. \tag{38}$$

We take the time derivative of equation (37) and inserting into it the divergence of equation (38), with the help of the Poisson equation we obtain an exact second-order non-linear differential equation describing the evolution of matter perturbations:

$$\ddot{\delta} + 2H\dot{\delta} - \frac{4}{3}\frac{\dot{\delta}^2}{1+\delta} - 4\pi G_{\rm eff}\bar{\rho}_{\rm m}\delta(1+\delta) = 0, \tag{39}$$

where $G_{\rm eff}$ is given by equation (35).

This is the non-linear equation we will use to infer the time evolution of the linear overdensity parameter δ_c. Its linearized version is

$$\ddot{\delta} + 2H\dot{\delta} - 4\pi G_{\rm eff}\bar{\rho}_{\rm m}\delta = 0, \tag{40}$$

reproducing the classical result, but with $G \to G_{\rm eff}$. It is worth pointing out that the correct linear growth has to be obtained from the non-linear equation for matter perturbations, equation (39). (For a more complete discussion on this point, we refer to Wintergerst & Pettorino 2010.) In order to evaluate the linear overdensity parameter δ_c, we use equation (39) to find the initial conditions δ_i and $\dot{\delta}_i$ such that δ diverges at the chosen time of collapse. Once the two initial conditions are found, we evolve them with the linear equation (40), and its density contrast at the collapse time gives δ_c.

Our main results are presented in Fig. 6. In the upper panel we show the time evolution of δ_c while in the lower panel we present the time evolution of Δ_V. We see that differences in δ_c are very small, much below 1 per cent at $z = 0$, while at high redshifts all the models converge to the Einstein–de Sitter (EdS) result. This is due to the stringent Solar system constraints which require a very weak coupling between the scalar field and the Ricci scalar. As seen in the lower panel of Fig. 1, gravity changes rapidly at low redshifts (where we expect the highest differences), while at high redshifts the gravitational constant G is practically constant and differs from the usual value by $\approx\pm 2$ per cent. We also notice that models with a lower (higher) growth factor also have a smaller (larger) δ_c. The NMC1 model is virtually indistinguishable from the ΛCDM model, while the largest differences appear for models with negative coupling (NMC2). Model MCH2 shows lower values for the linear overdensity parameter δ_c with respect to the ΛCDM model also at high redshifts. We checked that this is not the case at high redshifts, where it is expected to approach the behaviour of an EdS model.

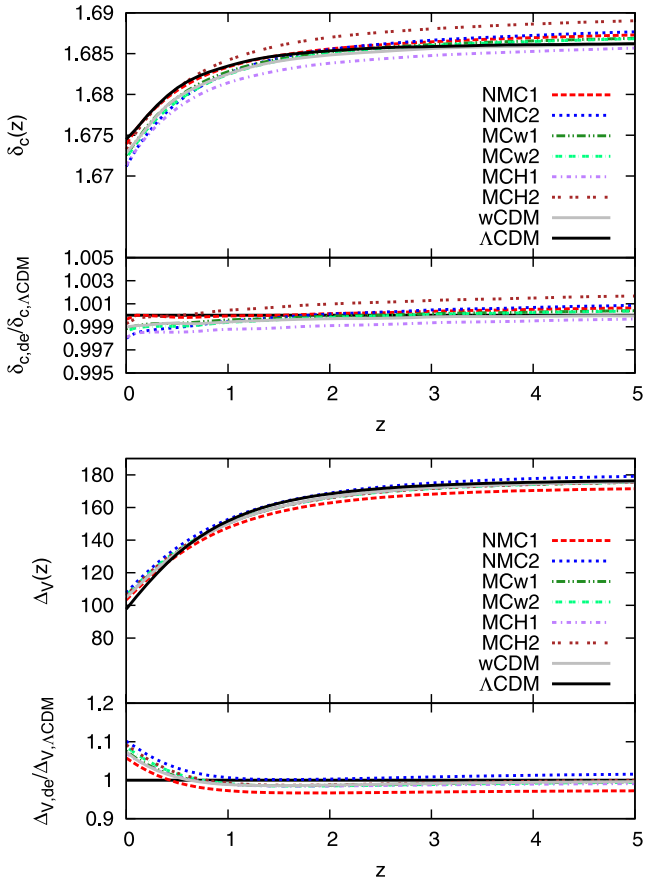

Figure 6. The redshift evolution of the linear overdensity parameter δ_c (top panel) and of the virial overdensity Δ_V (bottom panel) for the models here considered. Each panel consists of two insets: the upper one shows the absolute values of the quantities analysed, while the lower one the ratio between the dark energy models and the reference ΛCDM one. Line types and colours are as in Fig. 3.

In the lower panel of Fig. 6, we present results for the virial overdensity Δ_V. The virial overdensity is related to the non-linear evolution of the spherical overdensity. Given the turn-around scale factor a_{ta}, when the radius of the collapsing sphere reaches its maximum value and starts shrinking, the virial overdensity is defined as $\Delta_V = \delta_{nl} + 1 = \zeta(x/y)^3$, where $x = a/a_{ta}$ is the normalized scale factor and y is the radius of the sphere normalized to its value at the turn-around. For details on how to evaluate Δ_V and the radius of the sphere y, we refer the reader to Pace et al. (2010). The differences between the models studied here are also small, at most 10–15 per cent, once again largest at low redshifts. It is important to notice that at high redshifts, when naively we would expect to recover the result for the ΛCDM model, this does not happen for the models with strongest absolute coupling value (models NMC1 and NMC2); the differences are small in these cases, of order 2–3 per cent, but still appreciable. This kind of behaviour is expected, since Δ_V is related to the solution of the non-linear equation for overdensities (equation 39) and we expect that the models will strongly differ from each other at the non-linear level.

Here we have assumed that the traditional recipes available in literature to evaluate the virial overdensity are still valid [Wang & Steinhardt (1998)]. This should be valid here, since we assume the scalar field only modifies the background; however, this might not necessarily be the case if perturbations in the scalar field are accounted for.

It is interesting to notice that both at linear and non-linear level it is possible to see the effect of a time-dependent gravitational constant. In particular, for the linear overdensity parameter δ_c, while all the models show similar values, the minimally coupled models, except for the wCDM model, have a higher value with respect to the non-minimally coupled ones. The non-minimally coupled models have a very distinct signature: the lower is the value of the coupling constant, the lower is the linear overdensity parameter. A similar argument, albeit with reversed conclusions, applies to the non-linear virial overdensity.

The linear overdensity parameter δ_c is not directly observable, but it is an important quantity entering into the mass function. This subject will be discussed in the following section. The virial overdensity is instead related to the definition of observed clusters in order to define virial mass and virial radius. As seen before in the lower panel of Fig. 6, differences are small (<20 per cent), therefore, using the ΛCDM value will not result in a big error on the halo definition.

3.3 Mass function

We next discuss the mass function which describes the number of collapsed objects of a given mass that are formed at a given time in a unit volume. The mass function depends crucially on two factors: the linear growth factor $D_+(a)$ and the linear overdensity parameter δ_c. Since these quantities, or more precisely their ratio, appear quadratically in an exponential term, small deviations from the fiducial model can give rise to huge differences in the mass function. While δ_c is not an observable, the mass function, or its integral over the mass, can be directly observed using large cosmological surveys, once the survey selection functions are taken into account.

Another important ingredient for the mass function is the variance, defined via the relation

$$\sigma_M^2 = \frac{1}{2\pi^2}\int_0^{+\infty} k^2 T^2(k) W_R^2(k) P_0(k)\,\mathrm{d}k, \tag{41}$$

where $P_0(k)$ represents the primordial matter power spectrum, $T(k)$ is the matter transfer function and $W_R(k)$ is the Fourier transform of the real space top-hat window function. Since quintessence models differ slightly from the fiducial ΛCDM model (see e.g. Ma et al. 1999), for simplicity we assume that all the models have the same power spectrum shape, therefore, the only difference will be in the spectrum normalization. For the different values adopted, we refer to Table 1. To evaluate the mass function, we use the expression derived by Sheth & Tormen (1999).

To validate our work, we compare our theoretical predictions for the cumulative mass function with the simulation results by De Boni et al. (2011) at the same redshifts presented in their work, namely $z = 0, 0.5, 1$. In Fig. 7, we show the total number of objects in the simulated cube compared to the theoretical predictions. (For presentation purposes, we scaled the cumulative mass function of the model NMC1 and NMC2 by a factor of 5 and 25, respectively.) As it is clearly seen, at $z = 0$ (upper panel) we have a very good agreement between the theoretical predictions and the numerical results up to $5–6 \times 10^{14}\,M_\odot$, while for higher masses deviations are noticeable. This is expected, because in the simulations there are only very few objects in those mass bins, due to the fact that the simulated box size is only 300 Mpc h^{-1}. The error bars, as can be seen in fig. 6 in De Boni et al. (2011), are quite large and our theoretical expectations are well within the 1σ error bar.

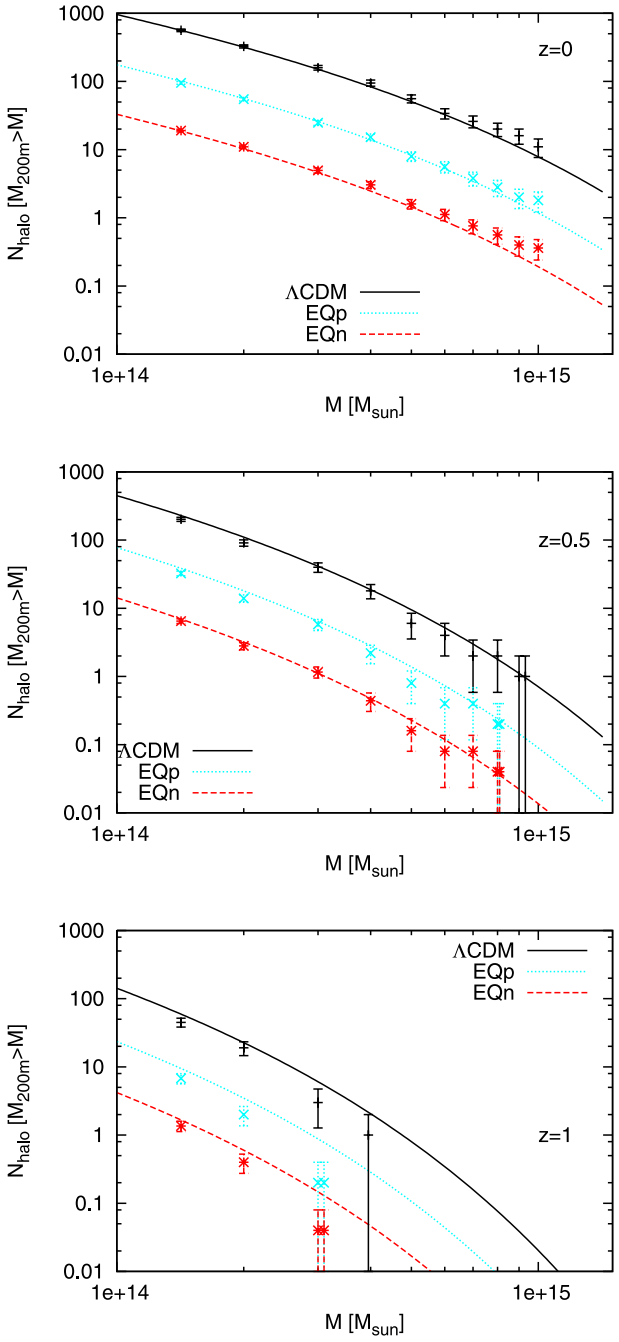

Figure 7. Comparison between the theoretical cumulative mass function and the results from *N*-body simulations. Black solid line and pluses represent the ΛCDM model, the cyan dotted line and crosses the EQp model (named NMC1 in this work) and red dashed line and stars the EQn model (named NMC2 in this work). Models EQp and EQn are scaled of a factor 5 and 25, respectively, for visualization purposes. Shown from top to bottom are comparisons at different redshifts: $z = 0$, 0.5 and 1.

At $z = 0.5$ (middle panel) the agreement between the theoretical predictions and the numerical mass function is still good over all the mass range available from the simulations. At $z = 1$ (lower panel), the agreement becomes substantially worse, especially for the two non-minimally coupled models. This is due to the lack of objects at that redshifts in the simulated volume; for the more numerous lower mass objects, up to $2 \times 10^{14}\,\mathrm{M}_{\odot}$, the agreement between simulations and analytic predictions remains good.

In Fig. 8 we show the ratio of the cumulative mass function for the dark energy models analysed with respect to the fiducial ΛCDM model. We evaluated the cumulative mass function, defined as the comoving number density of objects with mass exceeding M at different redshifts, at four different redshifts, namely $z = 0$, 0.5, 1 and 2.

By $z = 0$ the models have substantial differences from the ΛCDM model, in particular they all show fewer structures. As expected, largest differences occur in the high-mass tail, since rare events are affected more by changes in the growth of structure. Similar differences should appear in the void statistics. At $z = 0$, the differences range from 10 to 15 per cent for objects of mass $M \approx 10^{14}\,\mathrm{M}_{\odot}\,h^{-1}$ up to 40 per cent for very massive objects $M \approx 10^{15}\,\mathrm{M}_{\odot}\,h^{-1}$. At higher redshifts, the differences are even larger, in particular, at $z = 2$ the model NMC2 has about 20 per cent of the number of very massive objects compared to that seen in the ΛCDM model. Unfortunately at such high redshifts, the number of such massive clusters is so low that even large differences are difficult to observe unless a very large volume of space is observed.

Differences between the non-minimally coupled models increase much faster than differences between the corresponding minimally coupled models. In general, the minimally coupled models MCw1 and MCw2 show more structures than the corresponding non-minimally coupled models NMC1 and NMC2. The wCDM model, with constant equation of state, is one of the closest to the ΛCDM predictions. This shows how important the evolution of the dark energy equation of state parameter is for the mass function. As we are normalizing to the amplitude at early times, naively one might expect that the agreement with the ΛCDM model would be best at high redshifts, and in fact this is true for the MCH1 model. However, at higher redshifts one is looking further into the tails of the distribution for a fixed mass, making the mass function more sensitive to small changes in the growth of structure to that time. Because of the variation of the gravitational constant, the differences for the growth factor are higher for the non-minimally coupled models, therefore, the product $D_+(z)\sigma_8$ will be equal to the ΛCDM one at much higher redshifts. This is shown in Fig. 9 where we show the product $D_+(z)\sigma_8$ for the different models studied here for the redshift interval $0 \leq z \leq 2$. At higher redshifts massive objects are rare, therefore, a small variation in the quantities related to structure formation (growth factor and linear overdensity parameter) amplifies relative differences.

Many previous studies have dealt with alternative formulations of the halo mass function, based on fitting formulas of the numerical mass function in the *N*-body simulations and assuming as fundamental variable the variance of the linear matter power spectrum σ_{M} defined in equation (41) (see e.g. Jenkins et al. 2001; Reed et al. 2003, 2007; Warren et al. 2006; Tinker et al. 2008; Crocce et al. 2010; Courtin et al. 2011). These formulations differ mainly on the high-mass tail of the mass function and they could provide a higher fraction of massive objects.

In this work we adopt the prescription for the mass function following the work by Sheth & Tormen (1999). The reason for doing so is that the formulation of the mass function is motivated by the ellipsoidal collapse model and allowed us to verify the validity of our calculations in the framework of the spherical collapse model. It has therefore a well defined theoretical motivation, differently from the fitting formulas obtained for ΛCDM cosmologies, whose validity for different cosmological models is not obvious. In particular, the numerical parameters used to evaluate the mass function depend on the cosmological model studied and it is not obvious how to modify them for a new dark energy model without having to determine

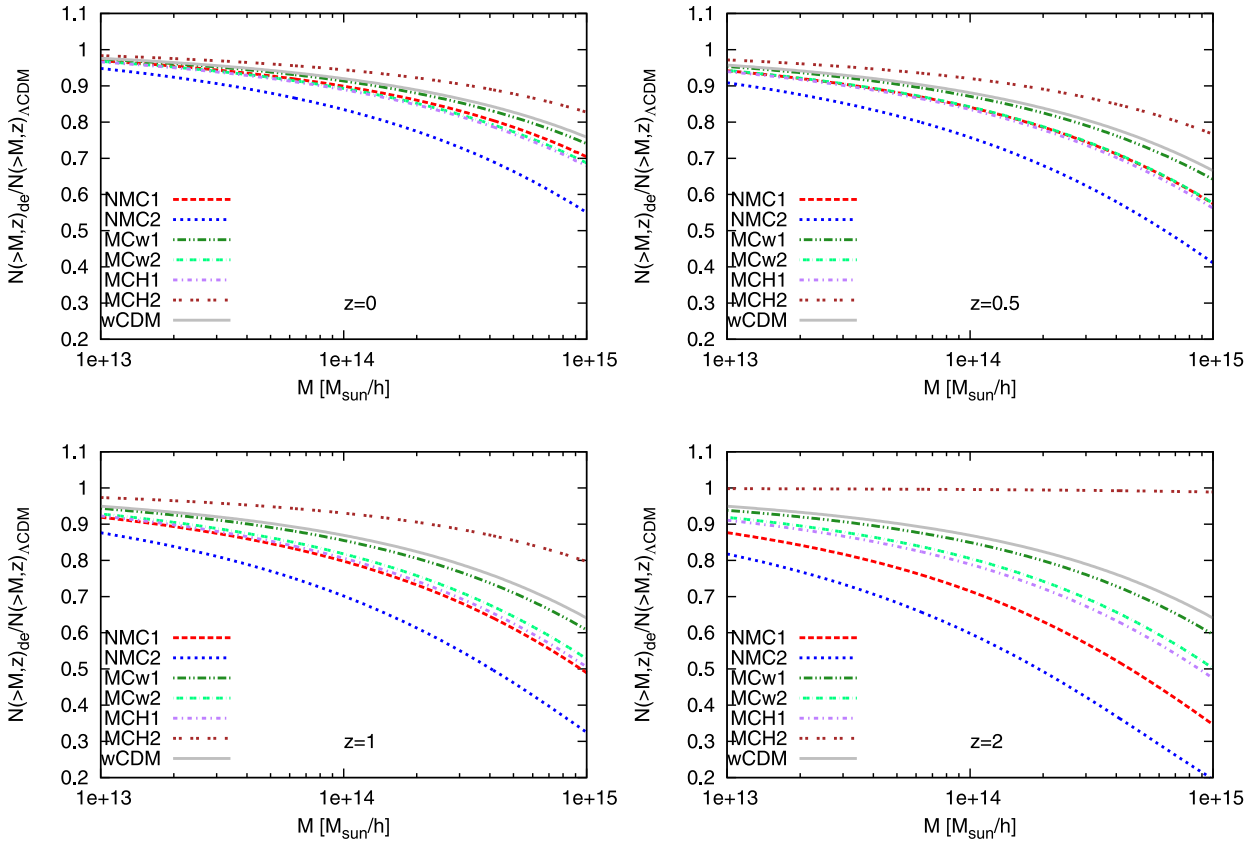

Figure 8. Cumulative comoving number density of objects with mass exceeding M at four different redshifts. Shown are ratios with respect to the reference ΛCDM model. Line types and colours are as in Fig. 3.

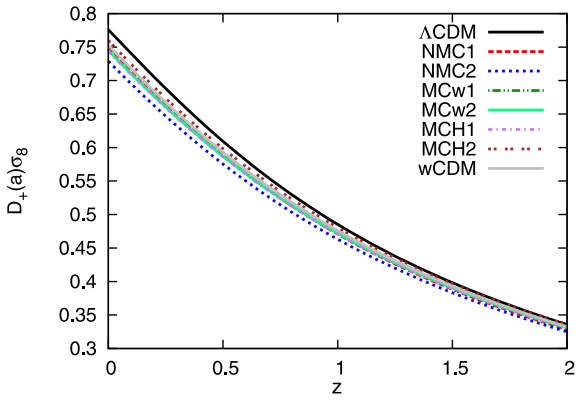

Figure 9. Time evolution of the variance σ_8 for the different models studied. The square of this quantity is important for the high-mass tail of the mass function. Labels are like in Fig. 3.

them again from new simulations. This introduces the problem of the non-universality of the mass function, deeply discussed in recent works by Lukić et al. (2007), Courtin et al. (2011) and Reed et al. (2013).

The interesting conclusion is that while a varying G impacts on structure formation more strongly than a simple non-minimally coupled dark energy model, one can infer differences between the models having the same background history only at high redshifts.

We will see in Section 3.5 how important this is when we study the cosmic shear power spectrum.

3.4 Dark matter power spectrum

A closely related statistic that can be used to study the dark matter clustering is the two-point correlation function $\xi(r)$ and its Fourier transform, the matter power spectrum. On large scales, in the linear or mildly non-linear regime, the power spectrum can be studied analytically, while for the fully non-linear regime it is necessary to use either numerical N-body simulations or semi-analytic prescriptions fitted against simulations (see e.g. Peacock & Dodds 1996; Smith et al. 2003). Such approaches are limited in their validity by the scales that can be reached by numerical simulations and on the models one can simulate. An alternative, physically motivated approach is given by the halo model developed by Ma & Fry (2000) and Seljak (2000) and others.

The halo model requires understanding in detail the mass function and the average dark matter density profile for a given model. Since these potentially depend on how the halo concentration changes with the coupling, it can be difficult to calibrate for non-minimally coupled models. However, it may be hoped that most of the physics will be captured in the ΛCDM model to first order, and in the following we will use power spectra obtained with the prescription of the halofit, as outlined in Smith et al. (2003). However, such uncertainties in the calibration must be kept in mind here and in the following section which relates to the shear power spectrum (see Section 3.5).

In Fig. 10 we show the ratio of the dark matter power spectrum for the quintessence models to the same quantity evaluated for the fiducial ΛCDM model as a function of the wavenumber. The matter power spectrum is evaluated at $z = 0$, using the CMB normalization

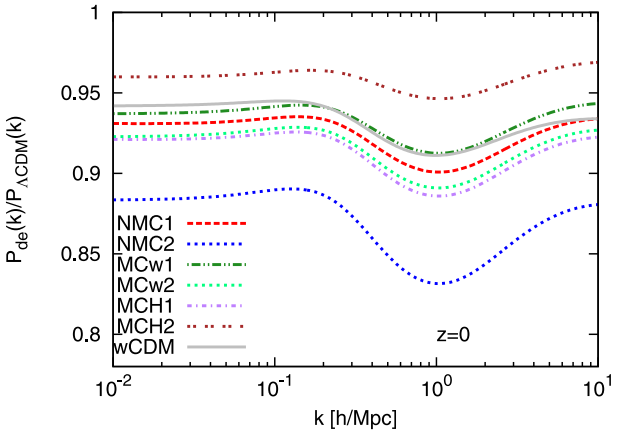

Figure 10. Non-linear dark matter power spectrum for $z = 0$ for the quintessence models here studied. Line types and colours are as in Fig. 3.

described in Section 2.3, where we refer for the exact normalization for each model. Using this normalization, the models have different power at all scales, which on linear scales results from integrating the different growth rates. As seen above, the largest differences arise for the NMC2 model while the model differing least is MCH2, as its normalization is very close to the ΛCDM one.

The differences from the fiducial ΛCDM model are highest at the scale of $k \approx 1h\,\mathrm{Mpc}^{-1}$, where the dynamical dark energy matter power spectra show a dip (see also Ma 2007). Since the power at all scales is significantly smaller than for the ΛCDM model, this results in a different scale where the power spectrum becomes non-linear and halofit corrections kick in. From a quantitative point of view, at large scales differences span a range between approximately 4 and 12 per cent to increase up to 16–17 per cent at $k \approx 1h\,\mathrm{Mpc}^{-1}$. The behaviour we found for the analytic power spectra is qualitatively in agreement with the analysis done by Fedeli, Dolag & Moscardini (2012) on the simulations presented by De Boni et al. (2011).

Nonetheless we see that our results differ quantitatively from their analysis. In particular, comparing our results with their model labelled DM_0, we see that in our case the models differ more from what is seen in the simulations of approximately 3 per cent (see the lower panels in their fig. 6). The major source of difference is related to the recipe we adopted to evaluate the full non-linear matter power spectrum. From our figure, it is evident that the halofit prescription can reproduce the non-linear behaviour of the power spectrum up to few per cent accuracy. We also notice that the offset between the halofit prescription and the numerical simulations is roughly constant for the different models analysed. Similarly to Fedeli et al. (2012), we also find that the dip slightly changes position when a different cosmological model is analysed. Moreover, as there speculated, the location of the dip is the same if the background history of the models does not change. This is indeed the case for the couple of models NMC1 and MCH1 and NMC2 and MCH2.

3.5 Cosmic shear power spectrum

Gravitational lensing, where the images of background objects are distorted gravitationally, is an essential tool for understanding the distribution of dark matter. Measurements of weak lensing, where the distortions to the shapes of objects are of order a few per cent or less, are straightforward to predict and interpret for cosmological models. One common weak lensing observable is the shear power spectrum, which is related to an integral along the line of sight of the matter power spectrum. To evaluate the modifications to the form of the shear power spectrum, we follow the approach of Tsujikawa & Tatekawa (2008) and Schimd, Uzan & Riazuelo (2005). Here we will just describe the most important steps in the derivation of the final formula and we refer to their papers for more details. For a detailed analysis on the general derivation of the lensing quantities for scalar–tensor theories, we refer to the work of Acquaviva et al. (2004). Recently, CMB lensing maps for a coupling in the Einstein frame that only involves dark matter were shown in Carbone et al. (2013).

Starting from the perturbed metric

$$\mathrm{d}s^2 = -(1+2\phi)\,\mathrm{d}t^2 + a^2(t)(1+2\psi)\delta_{ij}\,\mathrm{d}x^i\,\mathrm{d}x^j,$$

we can define the *deflecting potential*

$$\Phi_{\mathrm{wl}} = \phi + \psi, \tag{42}$$

and the effective density field

$$\delta_{\mathrm{eff}} = \frac{a}{3H_0^2\Omega_{\mathrm{m},0}}k^2\Phi_{\mathrm{wl}}, \tag{43}$$

where the relation between δ and δ_{eff} is given by

$$\delta_{\mathrm{eff}} = \frac{\delta_{\mathrm{m}}}{F}. \tag{44}$$

(Unlike in Tsujikawa & Tatekawa 2008, we do not have the term F_0 since in our case it is equal to one.) The magnification matrix is defined as

$$\boldsymbol{A}_{\mu\nu} = \boldsymbol{I}_{\mu\nu} - \int_0^{\chi}\frac{\chi'(\chi-\chi')}{\chi}\partial_{\mu\nu}\Phi_{\mathrm{wl}}\,\mathrm{d}\chi', \tag{45}$$

where χ is the comoving distance and I is the identity matrix; from this, the effective convergence is given by

$$\kappa = 1 - \frac{1}{2}\mathrm{tr}(A). \tag{46}$$

The shear power spectrum is related to the matter power spectrum by

$$P_\kappa(\ell) = \frac{9H_0^4\Omega_{\mathrm{m},0}^2}{4c^4}\int_0^{\chi_{\mathrm{H}}}\frac{W^2(\chi)}{a^2(\chi)F^2(a)}P_{\delta_{\mathrm{m}}}\left[\frac{\ell}{f_K(\chi)},\chi\right]\mathrm{d}\chi, \tag{47}$$

where $f_K(\chi)$ is the comoving angular diameter distance which depends on K, the spatial curvature of the universe, and $P_{\delta_{\mathrm{m}}}$ is the matter power spectrum analysed in Section 3.4. The integral in the previous equation formally extends up to the horizon size χ_{H}, however, since the number density of sources (see below) drops to zero much before that, the integral can be effectively truncated at $z \sim 10$. The kernel $W(\chi)$ is an integral over the source redshift distribution which must be inferred from observations. In the following we will adopt the source redshift distribution derived by Fu et al. (2008) using data from the Canada–France–Hawaii Telescope Legacy Survey (CFHTLS) and the parametrization for the non-linear matter power spectrum given by Smith et al. (2003), as discussed above.

In Fig. 11 we show the ratio of the cosmic shear power spectrum for the models studied with respect to the prediction of the ΛCDM model. These follow to a large extent the trends observed in the matter power spectrum (Fig. 10). On large scales power spectra differ from 6 to 13 per cent already, reflecting the normalization at high redshifts. The model with the smallest differences is MCH2, while the model with the highest differences is the model NMC2. As expected, deviations from the fiducial model increase towards smaller angular scales, where the effects due to non-linearity are more pronounced. The dip at $\ell \approx 10^3$ is a consequence of the analogous dip at $k \approx 1\,h\,\mathrm{Mpc}^{-1}$ seen in the power spectrum (see

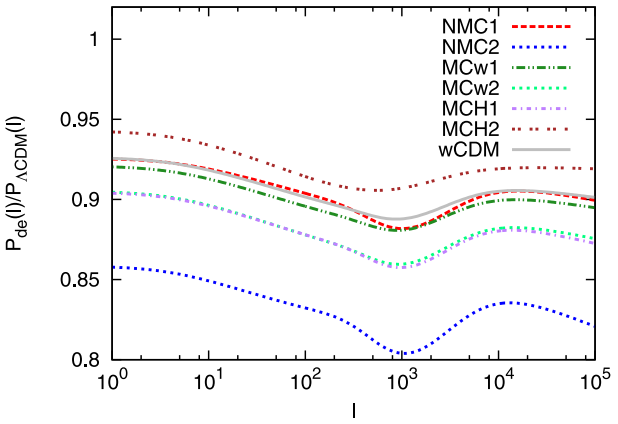

Figure 11. Weak lensing power spectrum for the models analysed in this work. We present the ratio with respect to the ΛCDM shear power spectrum. Line types and colours are as in Fig. 3.

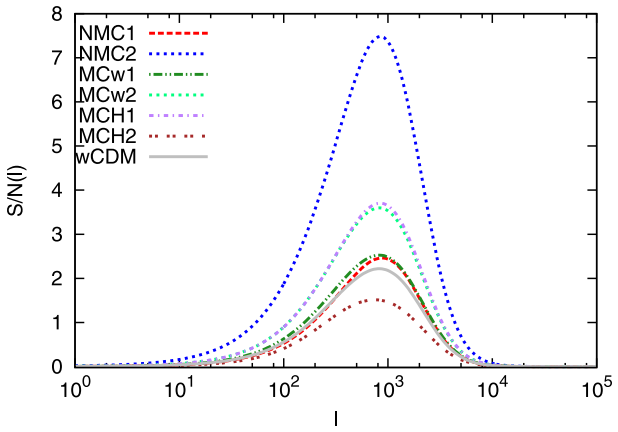

Figure 12. The S/N ratio to distinguish between the concordance cosmology and each of the quintessence models here considered as a function of the multipole. Line types and colours are as in Fig. 3.

Fig. 10). We stress that these results are valid only for multipoles up to $\ell \sim 2000$–3000 since for smaller angular scales we would have to take into account baryonic physics.

To see how likely it is to observe the differences between the models considered, we look at the signal-to-noise (S/N) ratio at a fixed multipole. The S/N ratio is defined as

$$\frac{\mathrm{S}}{\mathrm{N}}(\ell) = \left[\frac{P_\kappa^{\mathrm{DE}}(\ell) - P_\kappa^{\Lambda\mathrm{CDM}}(\ell)}{\Delta P_\kappa^{\Lambda\mathrm{CDM}}(\ell)}\right]^2, \tag{48}$$

where $\Delta P_\kappa^{\Lambda\mathrm{CDM}}(\ell)$ is the Gaussian statistical error on the power spectrum in the framework of the concordance cosmology. According to Kaiser (1992, 1998), Seljak (1998) and Huterer (2002), the latter can be evaluated approximately as

$$\Delta P_\kappa^{\Lambda\mathrm{CDM}}(\ell) = \sqrt{\frac{2}{(2\ell+1)\Delta\ell\, f_{\mathrm{sky}}}}\left[P_\kappa^{\Lambda\mathrm{CDM}}(\ell) + \frac{\gamma^2}{\bar{n}_{\mathrm{g}}}\right], \tag{49}$$

where $\bar{n}_{\mathrm{g}}$ is the average surface number density of observed galaxies, f_{sky} is the fraction of sky area surveyed and γ represents the rms intrinsic shape noise for the average galaxy. For practical purposes, we assume typical values for a future weak lensing survey and we set $\bar{n} = 40$ arcmin^{-2}, $f_{\mathrm{sky}} = 1/2$ and $\gamma = 0.22$ (see Zhang, Yuan & Lan 2009). As suggested by Takada & Bridle (2007) and Takada & Jain (2009) we use $\Delta\ell = 1$.

In Fig. 12 we show the S/N ratio for the cosmic shear power spectrum as a function of the multipole ℓ. We notice that at intermediate scales these models have a significant S/N ratio and that it decreases very quickly for lower and higher multipoles; this is in agreement with what was seen by Fedeli & Moscardini (2010) in the context of non-Gaussianity in weak lensing and Pace et al. (2012) in the context of oscillating dark energy models. This suggests that it will be very easy to differentiate the models via weak lensing techniques by summing just over few multipoles. Consistently with Fig. 11, the model with the highest S/N ratio is the NMC2, which differs most from the fiducial model.

A very important tool used to increase the power of cosmic shear is by using the tomography of lensing (Hu 1999; Takada & Jain 2004) and it consists in the subdivision of the sources in several bins, and computing the shear power spectrum in each bin and the cross-correlation between different redshift bins. More precisely, the cross-power spectrum between two bins is

$$P_\kappa^{ij}(\ell) = \frac{9H_0^4\Omega_{\mathrm{m},0}^2}{4c^4}\int_0^{\chi_{\mathrm{H}}} P\left(\frac{\ell}{f_K(\chi)}, \chi\right)\frac{W_i(\chi)W_j(\chi)}{a^2(\chi)F^2(a)}\mathrm{d}\chi, \tag{50}$$

and now the redshift distribution has to be normalized to unity in each redshift bin, rather than the whole redshift range.

We considered four different bins, close to the maximum number that should give appreciable improvement given the broad lensing kernel (Sun et al. 2009), using the redshift intervals [0, 0.5], [0.5, 1], [1, 1.5] and [1.5, ∞]. The results are shown in Fig. 13. In the bottom row we show the results for the ratio of the autocorrelation power spectra while in the other panels we present the cross-correlated power spectra. The label $m \times n$, where m and n run from one to four (total number of redshift bins), indicates the cross-correlation between bins m and n.

As it appears clear from Fig. 13 we notice that the information carried by the autocorrelation power spectrum is very similar for all the models. We see similar behaviour in the cross-correlated shear power spectrum. All the minimally coupled models behave very similarly and differ from the ΛCDM model of ≈10 per cent. As shown in Figs 11–13 differences between the dark energy models we consider are quite pronounced. According to Beynon et al. (2012), future lensing surveys as *Euclid*[2] (Laureijs et al. 2011; Amendola et al. 2013) will be able to differentiate models at the level of 2–3 per cent. Since all the models analysed here differ by the reference ΛCDM model for more than 5 per cent at all scales, we can safely conclude that future lensing surveys will easily say whether these models will be compatible with the data or not.

4 CONCLUSIONS

In this work we studied the structure growth and evolution of quintessence models, with particular emphasis on non-minimally coupled models (scalar–tensor theories) where the effective gravitational constant G changes in time. We compared representative scalar–tensor models to standard GR models which are described by the same equation of state, and also to a simple constant equation of state model ($w = -0.9$). We also considered two additional minimally coupled models where the background expansion is identical to the non-minimally coupled models. Our principle aim has been to isolate the influence of a varying gravitational constant G on structure formation, extending recent numerical work on this subject (De Boni et al. 2011) by carrying out analytic predictions for the same models that were previously simulated.

[2] www.euclid-ec.org

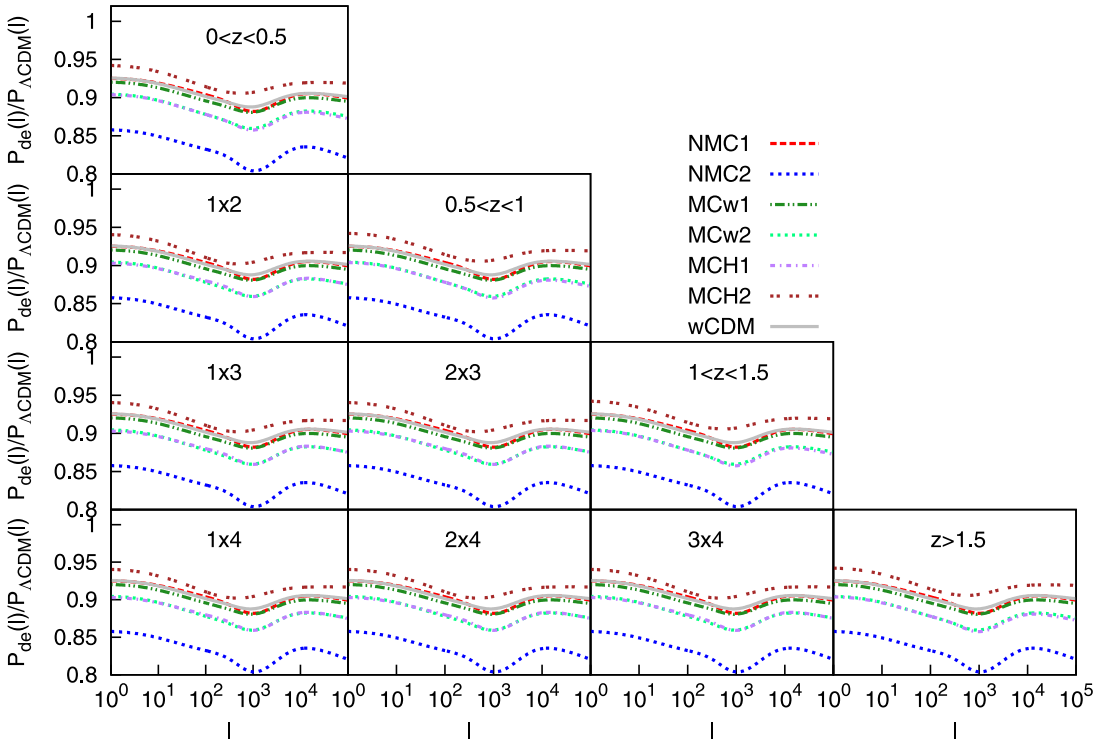

Figure 13. The cosmic shear power spectrum for the quintessence models here analysed derived in a specific source redshift bin. We present the ratio with respect to the predictions of the fiducial ΛCDM model. The redshift bins are as follows: $0 < z < 0.5$, $0.5 < z < 1$, $1 < z < 1.5$ and $1.5 < z < \infty$. The first three rows represent the cross-correlation power spectra, while the last row shows the autocorrelation power spectra. We refer to the labels in the panels for the corresponding redshift bins. Line types and colours are as in Fig. 3.

We studied several quantities, ranging from the linear analysis of the growth factor to the non-linearity of the mass function and of the weak lensing power spectrum. To validate our theoretical considerations, we compared our mass function to the one obtained directly from the *N*-body simulation (see Fig. 7). We showed that an analytical analysis of the linear growth factor ($D_+(a)$) and linear overdensity parameter δ_c can largely reproduce the numerical mass function over two orders of magnitude in mass.

A time-dependent G has a greater impact on all the quantities we considered, as compared to a conventional dark energy model whose dark energy component possesses the same equation of state, but interestingly enough, differences are mitigated, at least at the linear level, when the minimally coupled models have the same background expansion history predicted in the framework of scalar–tensor theory. The strength of gravity changes over time for scalar–tensor theories, adding one more degree of freedom to the standard general relativistic framework. In the models we considered G varied up to 2 per cent, leading to changes in background quantities at a similar level; however, at the perturbation level differences are amplified. For example, the growth factor can change up to 10 per cent and the range of variation is dictated by the models with the most extreme coupling (NMC1 and NMC2).

Similar comparisons can be made for the critical linear density contrast for spherical collapse $\delta_c(z)$ and the virial overdensity $\Delta_V(z)$. These remain similar to the predictions for a ΛCDM model, differing from it by only few per cent or less. As expected, the models converge to the prediction for an EdS universe at high redshifts, but the rate of convergence is model dependent and it is influenced by the amount of dark energy at early times.

These small differences are amplified when looking at the mass function for rare objects; differences from the fiducial model are large, of the order of 40 per cent for very massive objects already at $z = 0$ and can be as large as 80 per cent at a redshift $z = 2$, where one is probing even rarer objects. Deviations from the ΛCDM model are generally amplified if the gravity strength changes in time.

The dark matter power spectrum shows differences of the order of 10–15 per cent at most, particularly on mildly non-linear scales. On large scales differences are mostly due to integrated differences in the growth rate, ranging from 5 to 10 per cent. These conclusions are in qualitative agreement with those found by Fedeli et al. (2012) of the analysis of *N*-body simulations and differ by only a few per cent, showing that the usual recipes for the matter power spectrum can reproduce these models reasonably well without further calibration. The small differences are due to the fact that we assume that the assumptions used to build the halofit model are still valid in non-minimally coupled models (see discussion of how the non-linear matter power spectrum was evaluated in their section 4).

Finally, the effective convergence power spectrum is affected at the level of ∼10–15 per cent at intermediate/small angular scales. Since the corresponding observations are in principle very sensitive, it will be possible to discriminate these models with future lensing surveys, such as *Euclid*. In particular, as discussed in Beynon et al. (2012) a precision of few per cent can be reached. This implies that all the models could in principle be falsified if ΛCDM is the true cosmological model.

ACKNOWLEDGEMENTS

The authors thank Cristiano De Boni for providing the numerical mass function of their *N*-body simulations and Mischa Gerstenlauer, David Bacon and Emma Beynon for useful discussions. FP and RC are supported by STFC grant ST/H002774/1. VP is supported

by Marie Curie IEF, Project DEMO. LM acknowledges financial contributions from contracts ASI/INAF I/023/12/0, by the PRIN-MIUR09 'Tracing the Growth of Structures in the Universe' and by PRIN MIUR 2010-2011 'The Dark Universe and the Cosmic Evolution of Baryons: From Current Surveys to Euclid'.

REFERENCES

Abramo L. R., Batista R. C., Liberato L., Rosenfeld R., 2007, J. Cosmol. Astropart. Phys., 11, 12
Accetta F. S., Krauss L. M., Romanelli P., 1990, Phys. Lett. B, 248, 146
Acquaviva V., Baccigalupi C., Perrotta F., 2004, Phys. Rev. D, 70, 023515
Acquaviva V., Baccigalupi C., Leach S. M., Liddle A. R., Perrotta F., 2005, Phys. Rev. D, 71, 104025
Allen S. W., Schmidt R. W., Ebeling H., Fabian A. C., van Speybroeck L., 2004, MNRAS, 353, 457
Allen S. W., Rapetti D. A., Schmidt R. W., Ebeling H., Morris R. G., Fabian A. C., 2008, MNRAS, 383, 879
Amendola L., 2000, Phys. Rev. D, 62, 043511
Amendola L., 2004, Phys. Rev. D, 69, 103524
Amendola L., Quercellini C., Tocchini-Valentini D., Pasqui A., 2003, ApJ, 583, L53
Amendola L., Baldi M., Wetterich C., 2008, Phys. Rev. D, 78, 023015
Amendola L., Pettorino V., Quercellini C., Vollmer A., 2012, Phys. Rev. D, 85, 103008
Amendola L. et al., 2013, Living Rev. Relativ., 16, 6
Appleby S. A., Weller J., 2010, J. Cosmol. Astropart. Phys., 12, 6
Armendariz-Picon C., Mukhanov V., Steinhardt P. J., 2001, Phys. Rev. D, 63, 103510
Baccigalupi C., Matarrese S., Perrotta F., 2000, Phys. Rev. D, 62, 123510
Baldi M., Pettorino V., Robbers G., Springel V., 2010, MNRAS, 403, 1684
Banerjee N., Ganguly K., 2009, Int. J. Modern Phys. D, 18, 445
Barrow J. D., 1996, MNRAS, 282, 1397
Barrow J. D., Parsons P., 1997, Phys. Rev. D, 55, 1906
Bartelmann M., Doran M., Wetterich C., 2006, A&A, 454, 27
Bartolo N., Pietroni M., 2000, Phys. Rev. D, 61, 023518
Basilakos S., Sanchez J. C. B., Perivolaropoulos L., 2009, Phys. Rev. D, 80, 043530
Basilakos S., Plionis M., Solà J., 2010, Phys. Rev. D, 82, 083512
Bernardeau F., 1994, ApJ, 433, 1
Bertotti B., Iess L., Tortora P., 2003, Nat, 425, 374
Bett P., Eke V., Frenk C. S., Jenkins A., Helly J., Navarro J., 2007, MNRAS, 376, 215
Beynon E., Baldi M., Bacon D. J., Koyama K., Sabiu C., 2012, MNRAS, 422, 3546
Bludman S., 2004, Phys. Rev. D, 69, 122002
Boisseau B., 2011, Phys. Rev. D, 83, 043521
Boisseau B., Esposito-Farèse G., Polarski D., Starobinsky A. A., 2000, Phys. Rev. Lett., 85, 2236
Brans C., Dicke R. H., 1961, Phys. Rev., 124, 925
Bueno Sánchez J. C., Perivolaropoulos L., 2011, J. Phys. Conf. Ser., 283, 012006
Caldwell R. R., 2002, Phys. Lett. B, 545, 23
Carbone C., Baldi M., Pettorino V., Baccigalupi C., 2013, J. Cosmol. Astropart. Phys., 9, 4
Charmousis C., Copeland E. J., Padilla A., Saffin P. M., 2012, Phys. Rev. Lett., 108, 051101
Chiba T., 1999, Phys. Rev. D, 60, 083508
Clifton T., Barrow J. D., Scherrer R. J., 2005, Phys. Rev. D, 71, 123526
Coc A., Olive K. A., Uzan J.-P., Vangioni E., 2006, Phys. Rev. D, 73, 083525
Copeland E. J., Sami M., Tsujikawa S., 2006, Int. J. Modern Phys. D, 15, 1753
Courtin J., Rasera Y., Alimi J.-M., Corasaniti P.-S., Boucher V., Füzfa A., 2011, MNRAS, 410, 1911
Crocce M., Fosalba P., Castander F. J., Gaztañaga E., 2010, MNRAS, 403, 1353
De Boni C., Dolag K., Ettori S., Moscardini L., Pettorino V., Baccigalupi C., 2011, MNRAS, 415, 2758
Demarque P., Krauss L. M., Guenther D. B., Nydam D., 1994, ApJ, 437, 870
Eisenstein D. J. et al., 2005, ApJ, 633, 560
Esposito-Farèse G., Polarski D., 2001, Phys. Rev. D, 63, 063504
Farajollahi H., Salehi A., Nasiri M., 2011, Phys. Rev. D, 84, 124045
Faraoni V., 2000, Phys. Rev. D, 62, 023504
Fedeli C., Moscardini L., 2010, MNRAS, 405, 681
Fedeli C., Dolag K., Moscardini L., 2012, MNRAS, 419, 1588
Fu L. et al., 2008, A&A, 479, 9
Fujii Y., Maeda K.-I., 2003, The Scalar-Tensor Theory of Gravitation. Cambridge Univ. Press, Cambridge
Giannantonio T., Scranton R., Crittenden R. G., Nichol R. C., Boughn S. P., Myers A. D., Richards G. T., 2008, Phys. Rev. D, 77, 123520
Guendelman E. I., Kaganovich A. B., 2008, J. Phys. A: Math. Gen., 41, 164053
Haiman Z., Mohr J. J., Holder G. P., 2001, ApJ, 553, 545
Ho S., Hirata C., Padmanabhan N., Seljak U., Bahcall N., 2008, Phys. Rev. D, 78, 043519
Hoekstra H. et al., 2006, ApJ, 647, 116
Holden D. J., Wands D., 2000, Phys. Rev. D, 61, 043506
Hu W., 1999, ApJ, 522, L21
Huterer D., 2002, Phys. Rev. D, 65, 063001
Hwang J.-C., 1991, ApJ, 375, 443
Jaffe A. H. et al., 2001, Phys. Rev. Lett., 86, 3475
Jamil M., Raza M., Debnath U., 2012, Ap&SS, 337, 799
Jarosik N. et al., 2011, ApJS, 192, 14
Jarvis M., Jain B., Bernstein G., Dolney D., 2006, ApJ, 644, 71
Jenkins A., Frenk C. S., White S. D. M., Colberg J. M., Cole S., Evrard A. E., Couchman H. M. P., Yoshida N., 2001, MNRAS, 321, 372
Kaiser N., 1992, ApJ, 388, 272
Kaiser N., 1998, ApJ, 498, 26
Khoury J., Weltman A., 2004, Phys. Rev. D, 69, 044026
Komatsu E. et al., 2011, ApJS, 192, 18
Krauss L. M., Chaboyer B., 2003, Sci, 299, 65
Laureijs R. et al., 2011, preprint (arXiv:1110.3193)
Lee S., 2011, J. Cosmol. Astropart. Phys., 3, 21
Linder E. V., 2004, Phys. Rev. D, 70, 023511
Lukić Z., Heitmann K., Habib S., Bashinsky S., Ricker P. M., 2007, ApJ, 671, 1160
Ma Z., 2007, ApJ, 665, 887
Ma C.-P., Fry J. N., 2000, ApJ, 543, 503
Ma C.-P., Caldwell R. R., Bode P., Wang L., 1999, ApJ, 521, L1
Malquarti M., Copeland E. J., Liddle A. R., 2003, Phys. Rev. D, 68, 023512
Mashhoon B., Wesson P., Liu H., 1998, Gen. Relativ. Gravit., 30, 555
Matarrese S., Pietroni M., Schimd C., 2003, J. Cosmol. Astropart. Phys., 8, 5
Matarrese S., Baccigalupi C., Perrotta F., 2004, Phys. Rev. D, 70, 061301
Mota D. F., Barrow J. D., 2004, Phys. Lett. B, 581, 141
Mota D. F., van de Bruck C., 2004, A&A, 421, 71
Mota D. F., Shaw D. J., Silk J., 2008, ApJ, 675, 29
Nunes N. J., Mota D. F., 2006, MNRAS, 368, 751
Ohta Y., Kayo I., Taruya A., 2003, ApJ, 589, 1
Ohta Y., Kayo I., Taruya A., 2004, ApJ, 608, 647
Oyaizu H., 2008, Phys. Rev. D, 78, 123523
Pace F., Waizmann J.-C., Bartelmann M., 2010, MNRAS, 406, 1865
Pace F., Fedeli C., Moscardini L., Bartelmann M., 2012, MNRAS, 422, 1186
Peacock J. A., Dodds S. J., 1996, MNRAS, 280, L19
Percival W. J. et al., 2010, MNRAS, 401, 2148
Perivolaropoulos L., 2007, J. Phys. Conf. Ser., 68, 012005
Perlmutter S. et al., 1999, ApJ, 517, 565
Perrotta F., Baccigalupi C., 2002, Phys. Rev. D, 65, 123505
Perrotta F., Baccigalupi C., Matarrese S., 2000, Phys. Rev. D, 61, 023507
Perrotta F., Matarrese S., Pietroni M., Schimd C., 2004, Phys. Rev. D, 69, 084004
Pettorino V., Baccigalupi C., 2008, Phys. Rev. D, 77, 103003

Pettorino V., Baccigalupi C., Mangano G., 2005a, J. Cosmol. Astropart. Phys., 1, 14
Pettorino V., Baccigalupi C., Perrotta F., 2005b, J. Cosmol. Astropart. Phys., 12, 3
Pettorino V., Wintergerst N., Amendola L., Wetterich C., 2010, Phys. Rev. D, 82, 123001
Pettorino V., Amendola L., Baccigalupi C., Quercellini C., 2012, Phys. Rev. D, 86, 103507
Planck Collaboration et al., 2013a, preprint (arXiv:1303.5075)
Planck Collaboration et al., 2013b, preprint (arXiv:1303.5076)
Planck Collaboration et al., 2013c, preprint (arXiv:1303.5079)
Ratra B., Peebles P. J. E., 1988, Phys. Rev. D, 37, 3406
Reasenberg R. D. et al., 1979, ApJ, 234, L219
Reed D., Gardner J., Quinn T., Stadel J., Fardal M., Lake G., Governato F., 2003, MNRAS, 346, 565
Reed D. S., Bower R., Frenk C. S., Jenkins A., Theuns T., 2007, MNRAS, 374, 2
Reed D. S., Smith R. E., Potter D., Schneider A., Stadel J., Moore B., 2013, MNRAS, 431, 1866
Rees M. J., Sciama D. W., 1968, Nat, 217, 511
Riazuelo A., Uzan J.-P., 2002, Phys. Rev. D, 66, 023525
Riess A. G. et al., 1998, AJ, 116, 1009
Riess A. G. et al., 2004, ApJ, 607, 665
Riess A. G. et al., 2007, ApJ, 659, 98
Sachs R. K., Wolfe A. M., 1967, ApJ, 147, 73
Sahni V., Habib S., 1998, Phys. Rev. Lett., 81, 1766
Santiago D. I., Kalligas D., Wagoner R. V., 1997, Phys. Rev. D, 56, 7627
Schäfer B. M., 2008, MNRAS, 388, 1394
Schimd C., Uzan J.-P., Riazuelo A., 2005, Phys. Rev. D, 71, 083512
Schmidt H. J., 1990, Europhys. Lett., 12, 667
Schmidt F., 2009, Phys. Rev. D, 80, 043001
Seljak U., 1998, ApJ, 506, 64
Seljak U., 2000, MNRAS, 318, 203
Shaw L. D., Weller J., Ostriker J. P., Bode P., 2006, ApJ, 646, 815
Sheth R. K., Tormen G., 1999, MNRAS, 308, 119
Sidharth B. G., 2000, Nuovo Cimento B Ser., 115, 151
Smith R. E. et al., 2003, MNRAS, 341, 1311
Spergel D. N. et al., 2007, ApJS, 170, 377
Sun L., Fan Z.-H., Tao C., Kneib J.-P., Jouvel S., Tilquin A., 2009, ApJ, 699, 958
Takada M., Bridle S., 2007, New J. Phys., 9, 446
Takada M., Jain B., 2004, MNRAS, 348, 897
Takada M., Jain B., 2009, MNRAS, 395, 2065
Tegmark M. et al., 2004, Phys. Rev. D, 69, 103501
Tinker J., Kravtsov A. V., Klypin A., Abazajian K., Warren M., Yepes G., Gottlöber S., Holz D. E., 2008, ApJ, 688, 709
Torres D. F., 1995, Phys. Lett. B, 359, 249
Torres D. F., 2002, Phys. Rev. D, 66, 043522
Tsujikawa S., Tatekawa T., 2008, Phys. Lett. B, 665, 325
Tsujikawa S., Uddin K., Mizuno S., Tavakol R., Yokoyama J., 2008, Phys. Rev. D, 77, 103009
Unnikrishnan S., Seshadri T. R., 2008, Int. J. Modern Phys. D, 17, 2007
Uzan J.-P., 1999, Phys. Rev. D, 59, 123510
Vainshtein A. I., 1972, Phys. Lett. B, 39, 393
Vikhlinin A. et al., 2009, ApJ, 692, 1060
Wang L., Steinhardt P. J., 1998, ApJ, 508, 483
Wang S., Khoury J., Haiman Z., May M., 2004, Phys. Rev. D, 70, 123008
Wang J., Hui L., Khoury J., 2012, Phys. Rev. Lett., 109, 241301
Warren M. S., Abazajian K., Holz D. E., Teodoro L., 2006, ApJ, 646, 881
Wetterich C., 1985, Nucl. Phys. B, 252, 309
Wetterich C., 1988, Nucl. Phys. B, 302, 668
Wetterich C., 1995, A&A, 301, 321
Will C., 2001, Living Rev. Relativ., 4, 4
Wintergerst N., Pettorino V., 2010, Phys. Rev. D, 82, 103516
Zhang T.-J., Yuan Q., Lan T., 2009, New Astron., 14, 507
Zhao H., Macciò A. V., Li B., Hoekstra H., Feix M., 2010, ApJ, 712, L179
Zhao G.-B., Li B., Koyama K., 2011, Phys. Rev. D, 83, 044007

This paper has been typeset from a TEX/LATEX file prepared by the author.